Supporting Information

Note 1. The optical micrographs of the prepared samples

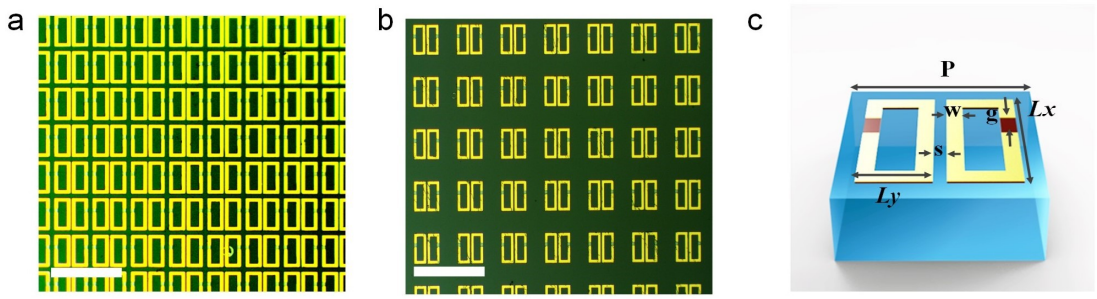

Figure S1. The optical micrographs of the prepared samples and detailed construction of meta-atom. (a) Sample 1 P = 53 μm (b) Sample 2 P = 80 μm (with a Scale bar of 100 μm) (c) meta-atom

As shown in Fig. S2c, the optimized structure and detailed parameters of the meta-atom are given as follows: L_x = 53 μm, L_y = 22 μm, w = 5.5 μm, s = 2.5 μm and g = 5 μm. And the coupling between lattice and double resonances is manipulated via the period variation.

Note2. The coupling of lattice to two resonances generated on static Si-metal hybrid metasurfaces

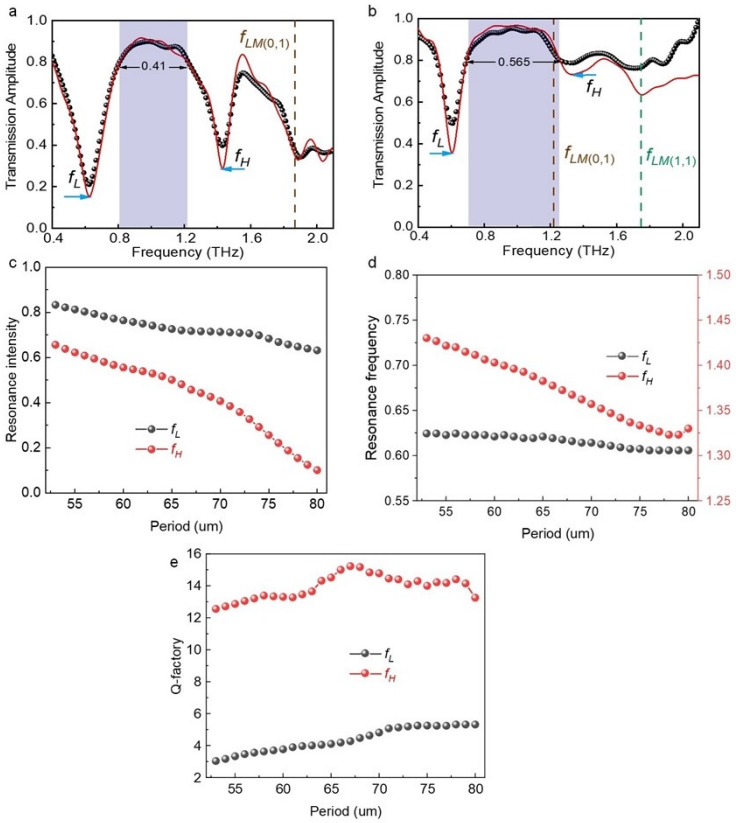

Figure S2. Transmission spectra and resonance properties with the growing period. Experimental and simulated transmission spectra (broadband transparent window marked in lavender) with (a) P=53 μm, (b) P=80 μm (c) Resonance intensity, (d) Resonance frequency, (f) Quality factor

The transmission spectra for P = 53, and 80 μm are shown in Fig. S2a, b, respectively. The red curves and black dots depict the simulated and experimental results, which match well with each other. And the deviations in resonance frequency, linewidth, and transmission amplitude are might due to the

low spectral resolution of the measurement and manufacturing imperfections. For the systematic exploration of the lattice mode impact on dual-resonances, the QF, resonance frequency, and intensity, varying by increased lattice periods with constant structure parameters otherwise, are shown in Fig. S2c, d, and e. The value of QF and the resonance intensity are obtained by $Q = \frac{f_0}{|f_{HM1} - f_{HM2}|}$ and $I = T_{peak} - T_{dip}$, where f_0 is the resonance frequency, f_{HM1} and f_{HM2} are the frequencies in which the transmission amplitude is half of the maximum value near f_0, T_{peak} and T_{dip} represent the peak and dip of transmission near f_0. Fig. S1d indicates the frequency shifts of f_L and f_H with varying lattice periods. For periods increasing from 53 to 80 μm, the f_H redshifts from 1.42 to 1.32 THz and then blueshifts to 1.33 THz when P= 80 μm. In contrast, the f_L is robust to the lattice period variations, which only weakly shift from 0.63 to 0.61 THz. In Fig. S1c, the intensity at f_L and f_H decreased from 0.83 and 0.66 to 0.63 and 0.10. Besides, the QF at f_H rises from 12.55 to 15.23 and then decreases to 13.26 after the perfect match between lattice modes with high-order resonance, as illustrated in Fig. S1e. However, the QF at f_L steadily increases from 3.03 to 5.32, with resonance intensity above 0.6.

Note 3. The relationship between the conductivity of silicon and pumping optical power

The measured negative differential transmission ($-\Delta E / E_0$) of silicon on sapphire with varying optical pumping power is shown in Fig.S3 a. The transient relaxation dynamics is theoretically fitted by an exponential decay function by:

$$-\frac{\Delta E}{E_0} = A_0 + A_1 \times e^{-\frac{(t-t_0)}{\tau}} \qquad (S1)$$

in which A_0 and A_1 are the constant and exponential parts of the silicon carriers dynamics process; t_0 and τ represent the start time for the relaxation decay and decay time constant. By theoretical fitting, the τ is calculated to be 247.6 ps. Next, the frequency-resolved photoconductivity $\Delta\sigma(\omega)$ could be obtained as

$$\Delta\sigma(\omega) = \frac{\varepsilon_0 c}{d}(n_a + n_b)\frac{E_0(\omega) - E_p(\omega)}{E_0(\omega)} \qquad (S2)$$

where ε_0 is the free space permittivity; c is the speed of light in free space; d is the thickness of silicon epitaxial layer; $E_0(\omega)$ and $E_p(\omega)$ is defined as the transmission of SOS without optical pump and different influences, respectively; n_a and n_b denotes refractive index of the sample on both sides. Fig.S3 b illustrates the measured frequency-resolved $\Delta\sigma(\omega)$ under changing pump fluences.

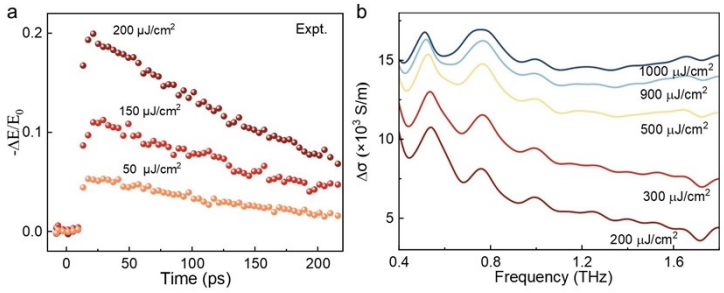

Figure S3. The relationship between the conductivity of silicon and optical pumping (a) Measured relaxation dynamics of silicon photogenerated carriers by OPTP with varying pump fluences (b) Frequency-resolved photoconductivity of silicon on sapphire with changing pump fluences.

Note 4. The near-field distribution of different metasurfaces with altering conductivities

To explore the intrinsic mechanisms of optical modulation, the electrical field, Z component of the magnetic field and surface current distribution at different frequencies with various silicon conductivity are shown in Figure S4. Considering the resemblance in the transmission spectra with various lattice periods, we exhibit the near-field distribution at f_L, f_H and the peak frequency of BTTW (f_M=0.9 THz) with different silicon conductivity when P =53 μm. With S=160 S/m, a strong local electric field is generated at the gap of SRRs at f_L and f_M, while horizontally distributed in the inner of square rings at f_H. And the toroidal dipole and quadrupole appear at f_L, f_M and f_H, respectively. Moreover, the surface current distribution demonstrates the presence of an electric dipole at f_L and f_M, whereas an electric quadrupole at f_H. As a result, the low-order resonance at f_L and f_M mainly comprises electric and toroidal dipole, while the high-order at f_H consists of the electric and toroidal quadrupole. Increasing the conductivity to simulate growing optical pumping fluences, the photogenerated carriers from the silicon induce a capacitive breakdown of the gaps, resulting in field remodeling. As a result, the surface current distribution, electric, and Z component of the magnetic field is significantly weakened at f_L and f_M, whereas a slight attenuation occurs at f_H.

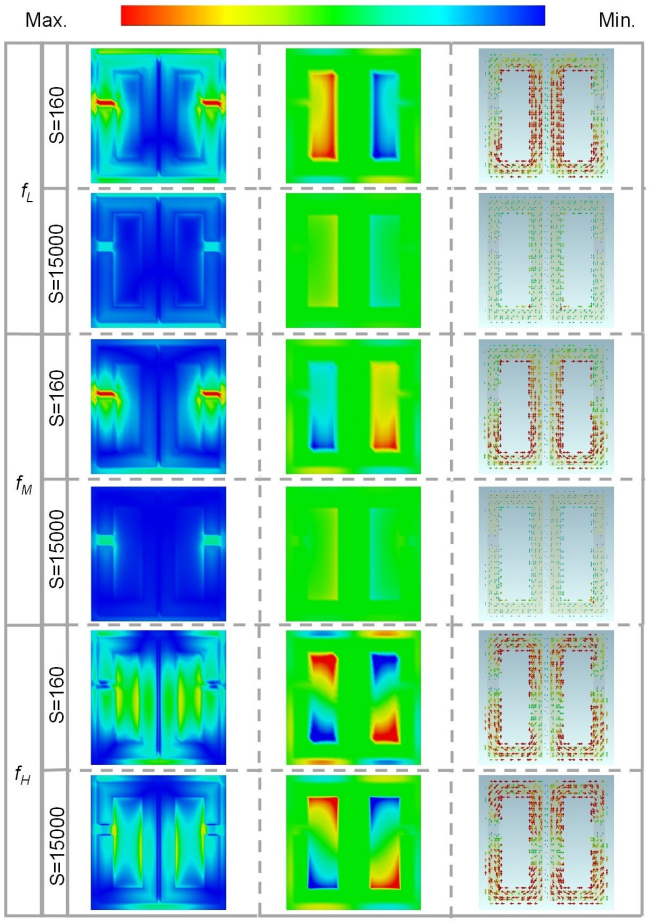

Figure S4. The electrical field, Z component of magnetic field and surface current distribution at different frequencies with various conductivity of silicon. (a)-(c) S = 160 at f_L (d)-(f) S = 15000 at f_L (g)-(i) S = 160 at f_M (j)-

(h) S = 15000 at f_M (m)-(o) S = 160 at f_H (p)-(r) S = 15000 at f_H

Note 5. The relationship between lattice and the scattering intensity of multiple radiating polarons

Relying on multipole decomposition, an approach to calculate multipole moments scattering intensity by integrating the current and charge density, we present a more in-depth understanding of the interaction between lattice mode and dual-resonances. The main types of multipole moments, including $\boldsymbol{P}$ (electric dipole moment), $\boldsymbol{T}$ (toroidal dipole moment), $\boldsymbol{M}$ (magnetic dipole moment), $\boldsymbol{Q}^{(e)}_{\alpha,\beta}$ (electric quadrupole moment), and $\boldsymbol{Q}^{(m)}_{\alpha,\beta}$ (magnetic quadrupole moment), are considered. And the multipole moments and corresponding scattering intensities are calculated in the Cartesian coordinate system ($\alpha, \beta = x, y, z$) by

$$
\begin{aligned}
\boldsymbol{P} &= \frac{1}{i\omega}\int \boldsymbol{J}d\boldsymbol{r} \\
\boldsymbol{T} &= \frac{1}{10c}\int [(\boldsymbol{r}\mathrm{g}\boldsymbol{J})\boldsymbol{r} - 2\boldsymbol{r}^2\boldsymbol{J}]d\boldsymbol{r} \\
\boldsymbol{M} &= \frac{1}{2c}\int (\boldsymbol{r}\times\boldsymbol{J})d\boldsymbol{r} \\
Q^{(e)}_{\alpha,\beta} &= \frac{1}{2i\omega}\int [r_\alpha J_\beta + r_\beta J_\alpha - \frac{2}{3}\delta_{\alpha,\beta}(\boldsymbol{r}\mathrm{g}\boldsymbol{J})]d\boldsymbol{r} \\
Q^{(m)}_{\alpha,\beta} &= \frac{1}{3c}\int [(\boldsymbol{r}\times\boldsymbol{J})_\alpha r_\beta + (\boldsymbol{r}\times\boldsymbol{J})_\beta r_\alpha]d\boldsymbol{r}
\end{aligned}
\tag{2}
$$

$$
\begin{aligned}
I_P &= \frac{2\omega^4}{3c^3}\left|\boldsymbol{P}\right|^2 \\
I_T &= \frac{2\omega^6}{3c^3}\left|\boldsymbol{T}\right|^2 \\
I_M &= \frac{2\omega^4}{3c^3}\left|\boldsymbol{M}\right|^2 \\
I_{Q^{(e)}} &= \frac{\omega^6}{5c^5}\left|\boldsymbol{Q}^{(e)}_{\alpha,\beta}\right|^2 \\
I_{Q^{(m)}} &= \frac{\omega^6}{20c^5}\left|\boldsymbol{Q}^{(m)}_{\alpha,\beta}\right|^2
\end{aligned}
\tag{3}
$$

where $\boldsymbol{r}$ and $\boldsymbol{J}$ is the position vector and the current density. For a visual representation of the interaction between lattice mode and multipole moments, it is necessary to note that we normalized the scattering intensities by $I^{Pi}_{\gamma} = \frac{I^{Pi}_{\gamma}}{I^{P_0}_{\gamma}}$ $(\gamma = \boldsymbol{P}, \boldsymbol{M}, \boldsymbol{T}, \boldsymbol{Q}^{(e)}, \boldsymbol{Q}^{(m)})$ due to the enormous difference of magnitude order in the scattering intensity between various polar moments, which I^{Pi}_{γ} and $I^{P_0}_{\gamma}$ represent the scattered intensity at *pi* and p_0 (p_0 = 53 μm). As demonstrated in Fig. S3f, the lattice mode $f_{LM(0,1)}$ (Brown line) and $f_{LM(1,1)}$ (Green line) redshift by increasing periods, accompanied by a narrowing transmission valley and frequency shift at f_L and f_H. To explain this phenomenon, the normalized

scattering intensities for multipole moments are shown in Figures 5a-e, with the resonance at f_L and f_H marked by black dashed boxes considering the frequency shifts.

Besides, we also summarize the lattice effects on resonance as follows: (i) As dark modes, lattice coupling with bright modes is universal, which impacts not only the resonance near fLM but also the ones ahead. (ii) With increasing periods, the match/mismatch between lattice mode and resonance enhances/weakens the LMI at the direct coupled mode and consistently enlarges the QF at the indirect one with a relatively great resonance intensity. (iii) The match of lattice mode would enhance the radiation properties of the moments at the resonant frequency, including $\boldsymbol{P}$, $\boldsymbol{M}$, $\boldsymbol{T}$, $\boldsymbol{Q}^{(e)}_{\alpha,\beta}$ and $\boldsymbol{Q}^{(m)}_{\alpha,\beta}$, to boost the LMI. It is demonstrated that the slight sacrificing of compactness could enhance resonance without changing the pattern above the substrate and offer a counter-conventional paradigm for high QF device design, LMI enhancement, and nonlinear optics.

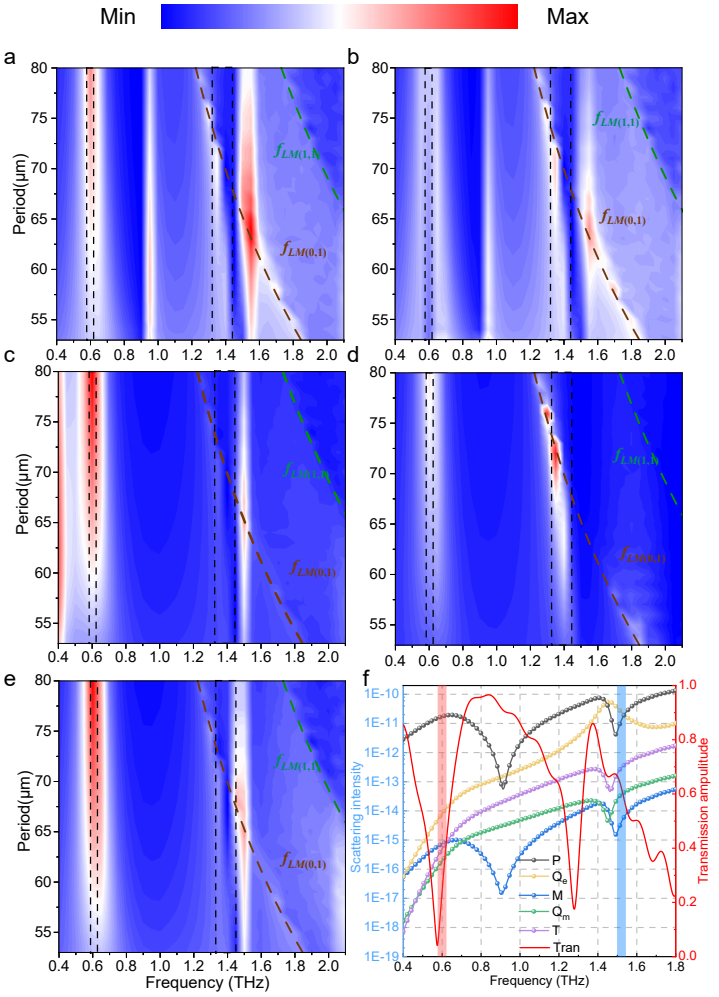

Figure S5. Normalized scattering intensity of multipole moments including $\boldsymbol{P}$, **T**, **M**, $\boldsymbol{Q}^{(e)}_{\alpha,\beta}$, and $\boldsymbol{Q}^{(m)}_{\alpha,\beta}$ with increasing lattice periods. The green and brown dashed curves signify the lattice mode $f_{LM(0,1)}$ and $f_{LM(1,1)}$, respectively. (a) the electric dipole moment $\boldsymbol{P}$ (b) the magnetic dipole moment $\boldsymbol{M}$ (c) the toroidal dipole moment $\boldsymbol{T}$ (d) the electric quadrupole moment $\boldsymbol{Q}^{(e)}_{\alpha,\beta}$ (e) the magnetic quadrupole moment $\boldsymbol{Q}^{(m)}_{\alpha,\beta}$ (f) the multipole scattering

intensity with corresponding resonance.

Note 6. Removal of Water Vapor Errors by Self-Calibration Normalization.

The THz waves interact with water vapor during airborne transmission, leading to errors in both the time and frequency domains. Here, the water vapor error can be eliminated by self-calibration before and after the ultrafast photodynamic process. Assuming that the thickness of the test sample is *d*, the total transmission distance is $\Delta L + d$, the mathematical expression for the signal with the noise of carrying water vapor after passing through the sample is as follows:

$$E(v)_{sam+vap} = E(v)_{nitrogen} t_{as} t_{sa} \exp(\frac{-j2\pi v \tilde{n}_s(v) d}{c}) \times \exp(\frac{\Delta L \alpha(v)}{2}) \exp(\frac{-j2\Delta L \pi v n(v)}{c})$$

where t_{as} and t_{sa} are the transmission efficiencies from air to sample and from sample to air, respectively, $\tilde{n}_s(v)$ and $n(v)$ are the effective reflection coefficients of the sample and water vapor, respectively, and $\alpha(v)$ is the absorption coefficient of water vapor. In conventional calibration methods, the measurement error will increase due to sample thickness and ambient humidity:

$$W(v)_{erro} = \exp(-\frac{d\alpha(v)}{2}) \exp(\frac{-j2d\pi v n(v)}{c})$$

With optical pumping, the electric field vector of the transmitted signal can be expressed as:

$$E(v)'_{sam+vap} = E(v)_{nitrogen} t'_{as} t'_{sa} \exp(\frac{-j2\pi v \tilde{n}_s(v) d}{c}) \times \exp(\frac{\Delta L \alpha(v)}{2}) \exp(\frac{-j2\Delta L \pi v n(v)}{c})$$

The normalized target sample signal is

$$\begin{aligned} E(v)_{sc} &= E(v)_{sam+vap} / E(v)'_{sam+vap} \\ &= \frac{t_{as} t_{sa}}{t'_{as} t'_{sa}} \exp(\frac{-j2\pi v [\tilde{n}_s(v) - \tilde{n}_s(v)] d}{c}) \end{aligned}$$

Hence, the error introduced by water vapor is completely eliminated.

Note 7. The verification of lattice enhancement for light-driven modulators.

To demonstrate the lattice enhancement effect, we have simulated the ultrafast optical modulator [1] proposed by **Hu et al.** via the finite time domain difference method (FDTD). As illustrated in Figure S6a, X and Y directions were assumed as periodic boundary conditions, and the plane-wave with an X-polarized electric field was directed towards the metasurfaces along Z direction (Set as an open boundary). The transmission spectrum and multipole analysis for $P = 60\ \mu m$ is shown in Figure S6c. The f_L (low-frequency resonance) and f_H (high-frequency resonance) appear at 1.2 and 2.3 THz, respectively, originating in dipole-dominated strong scattering. With increasing periods, the lattice mode $f_{LM(0,1)}$ blueshifts to match\mismatch with f_L, and $f_{LM(1,1)}$ blueshifts to coupling to f_H and f_L successively, leading to the narrowing of resonances. It is worth noting that the f_L does not disappear with the mismatch because the lattice is only an aid for the bright resonance. The normalized scattering intensities of multipoles are demonstrated in Figure S7. All the scattering intensities of multipoles are increased with the strengthening of lattice coupling, coinciding with the universality of lattice enhancement effect. However, the scattering intensities of $\boldsymbol{T}$ and $\boldsymbol{Q}_{\alpha,\beta}^{(m)}$ are still boosted owing to the matching of $f_{LM(1,1)}$, when $f_{LM(0,1)}$ mismatches with f_L.

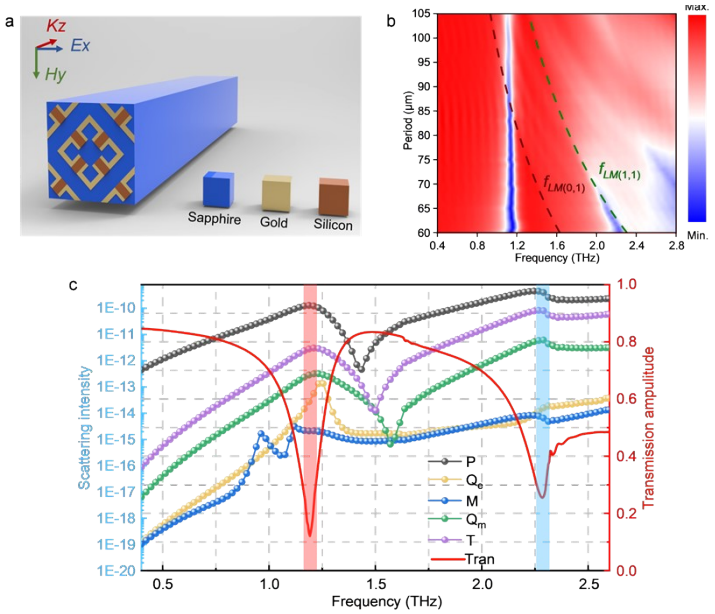

Figure S6. The schematic diagram of simulation and the transmission spectrum (a) Simulated details in FDTD (b) Transmission spectrum with varying periods (c) The transmission spectrum and multipole analysis results for $P = 60\ \mu m$

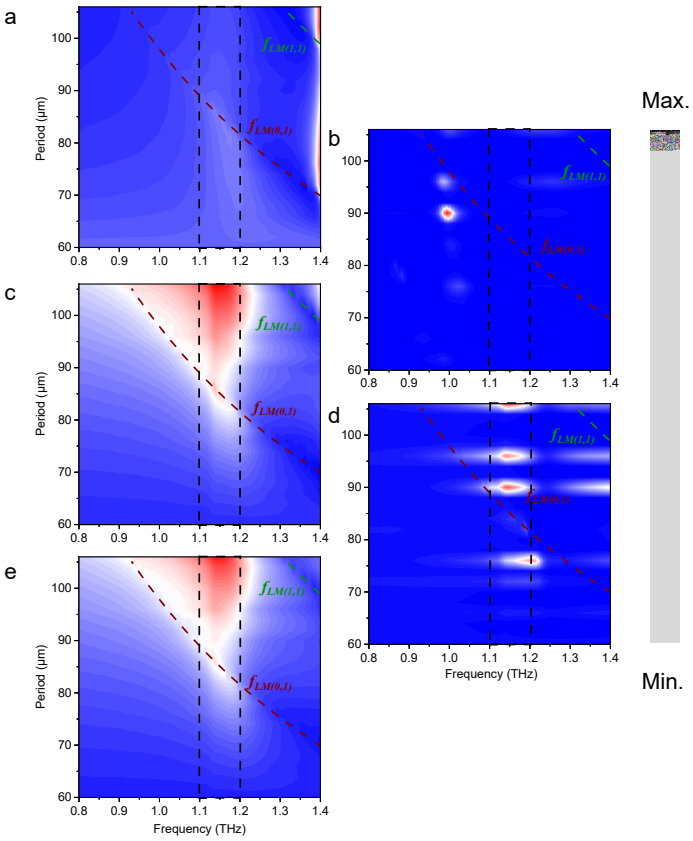

Figure S7. The normalized scattering intensity of multipoles (a) the electric dipole moment $\boldsymbol{P}$ (b) the magnetic dipole moment $\boldsymbol{M}$ (c) the toroidal dipole moment $\boldsymbol{T}$ (d) the electric quadrupole moment $\boldsymbol{Q}^{(e)}_{\alpha,\beta}$ (e) the magnetic

quadrupole moment $\boldsymbol{Q}_{\alpha,\beta}^{(m)}$

Furthermore, the tunable performance of modulators with different periods is investigated. The conductivity of silicon is regularly changed in simulation to mimic varying optical pumping. The modulated properties for $P = 65$, 73, and 90 μm are shown in Figure S8. Consistency with the results [1], the f_L is intensely suppressed by growing pump fluence because of conducted silicon bridge. Meanwhile, the device could modulate slow-light behaviors, characterized by a pronounced group delay switching. As presented in our paper, the modulated performance, including transmission and group delay modulation, shows significant variations for different periods. The simulated results of modulated performance with varying periods are shown in Figure S9 for a clear comprehension of the lattice effect on modulators. The transmission modulation strengthens from 0.48 to 0.55 and then decreases to 0.29 with increasing periods, while the slow light behaviors are consistently suppressed.

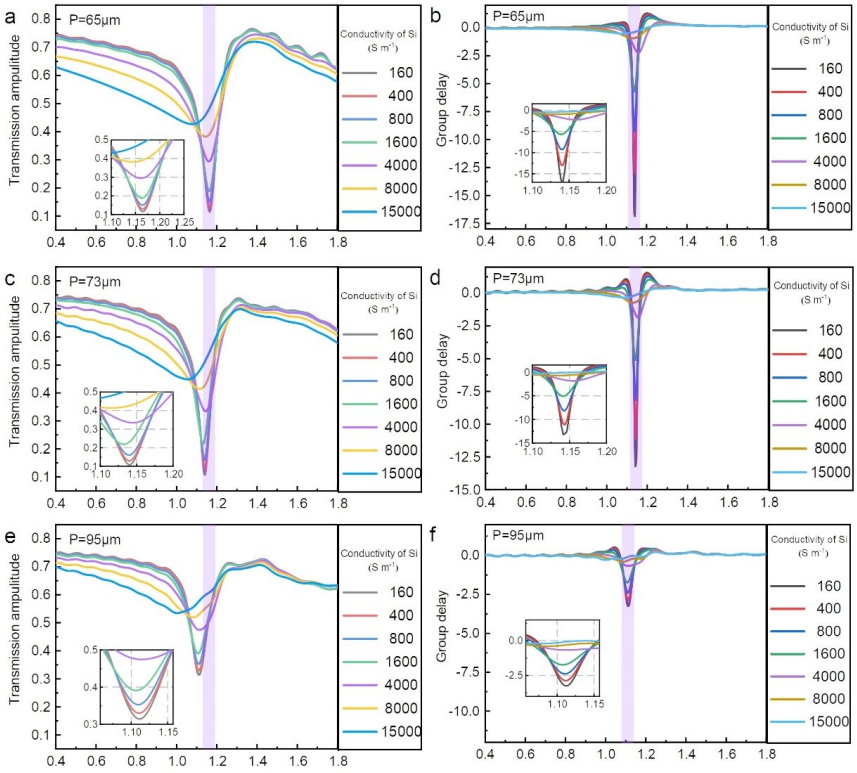

Figure S8. The transmission properties and slow light behaviors with varying pumping fluence for different periods (a), (c), and (e) transmission spectrum and (b), (d), and (f) group delay spectrum with lattice periods (a, b) $P = 65$ μm, (c, d) $P = 73$ μm, and (e, f) $P = 95$ μm

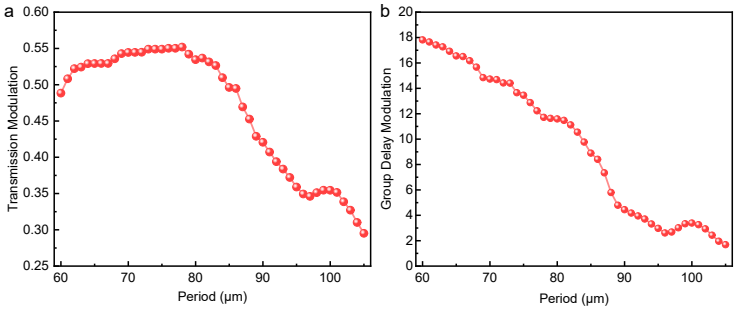

Figure S9. The tunable performance with different periods. (a) the transmission modulation (b) the group delay

modulation

Note 8. The difference between structural parameters and lattice periods.

We investigated the modulated performance of light-driven devices with different structural parameters (*s* and *g*), which is demonstrated in Figure S10. Clearly, the f_L and f_H blue shift with increasing *s* or *g*, and possess varying modulated depth (In Figures S10c, and f). However, the trends of varying modulated depth are irregular, which will increase the time for device optimization. Besides, the apparent frequency shifts might be harmful to the desired working point compared with lattice enhancement. In other words, for potential modulation of performance at fixed resonant frequency, several structural parameters should be adjusted.

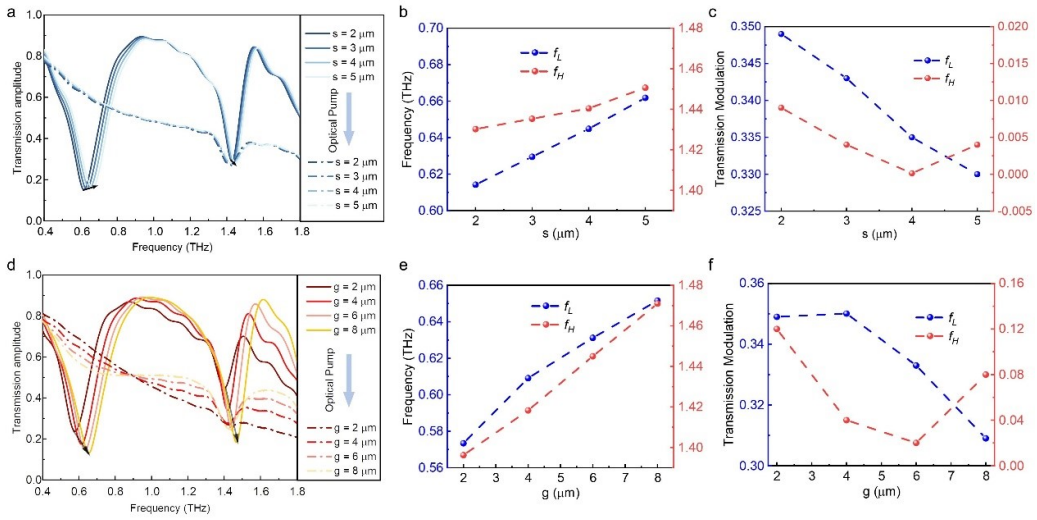

Figure S10. The varying performance of light-driven modulators with changing structural parameters. The changing transmission characteristics with different *s* (a) Transmission spectrum (b) Frequency shifts (c) Modulated depth. The corresponding results with changing *g*. (d) Transmission spectrum (e) Frequency shifts (f) Modulated depth.

Note 9. The sensing performance for detected substance with different thicknesses.

To demonstrate the sensing performance for substances with different thicknesses, we have investigated the change of self-calibrating normalized transmission. As shown in Figure S11, the refractive index sensing performance of the device is enhanced with growing thicknesses, which is due to the increased contact volume between the substances and the electromagnetic field.

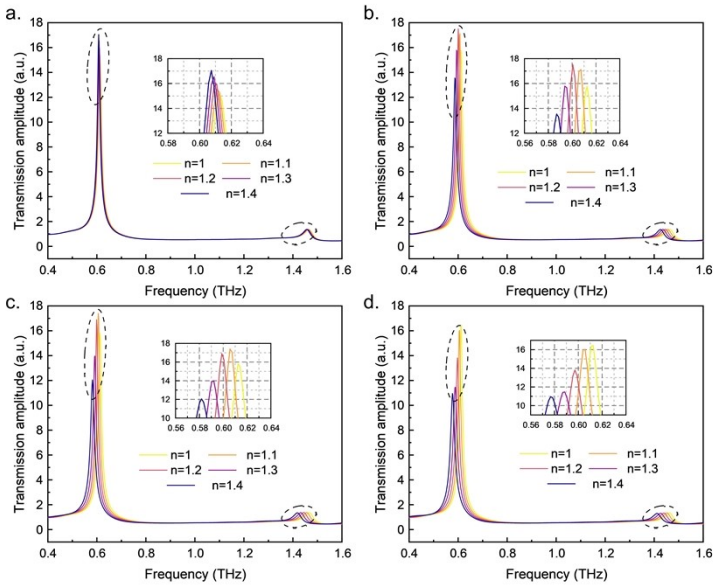

Figure S11. The refractive index sensing performance for different thicknesses of detected substances. (a) Detects thickness of 1 μm (b) Detects thickness of 5 μm (c) Detects thickness of 10 μm (d) Detects thickness of 20 μm.

The sensing performance for different detected substances is demonstrated in Figure S12, which is firstly enhanced with increased thicknesses. However, unlike the sensing performance to refractive index, the loss sensing performance reaches an optimum and then decreases with continuously increasing thicknesses.

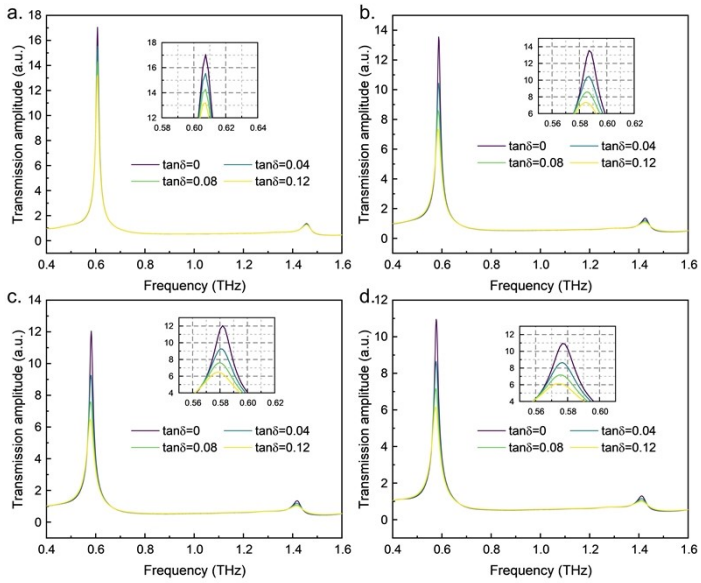

Figure S12. The loss sensing performance for different thicknesses of detected substances. (a) Detects thickness of 1 μm (b) Detects thickness of 5 μm (c) Detects thickness of 10 μm (d) Detects thickness of 20 μm.

Note 10. The influence of oblique EM waves on metadevice.

As shown in Figure S13, we have simulated the transmission spectrum for unexcited/excited metadevice with P = 53 μm. In Figures S13a and b, for the EM waves incident on the small angle, both the resonant intensity and frequency of unexcited/excited metadevice of f_L and f_M, remain stable, while

slightly changing at f_H. However, the resonant intensity of f_L, f_M, and f_H significantly changes for oblique EM waves in big angles. The resonance red shifts at f_H while remaining at f_L. In conclusion, the metadevice exhibits angular robustness for oblique EM waves, which is beneficial for realistic application.

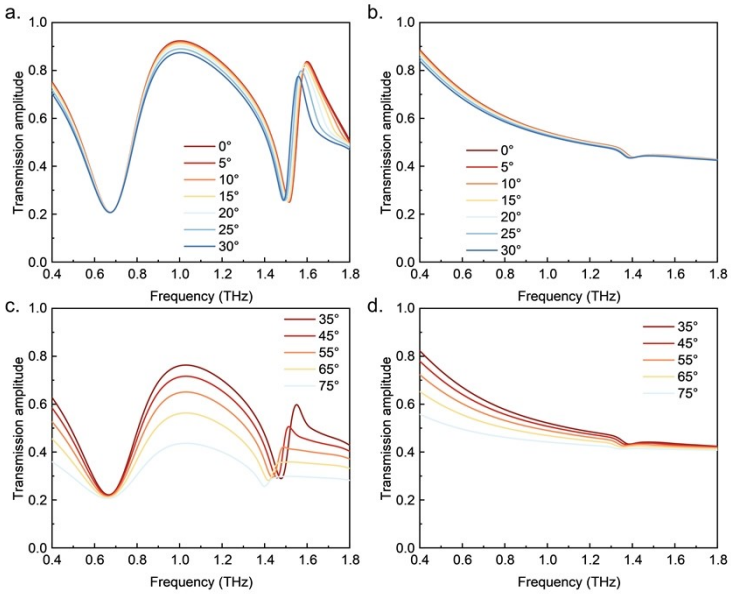

Figure S13. The transmission spectrum of unexcited/excited metadevice with oblique EM waves. (a) Unexcited metadevice with oblique EM waves in small angle (b) Excited metadevice with oblique EM waves in small angle (c) Unexcited metadevice with oblique EM waves in big angle (d) Excited metadevice with oblique EM waves in big angle.

Note S11. The mutual correlation among multiple functions based on silicon-metal hybrid metasurfaces

As shown in Figs2 f-g and Figs3 f-g in the main text, the resonance attenuation/enhancement at f_L and f_H occur simultaneously with a stable group delay switch at BTW under optical pumping. There is consistency among multiple functions, implying that it is impossible to achieve a single function in isolation. Furthermore, in Figs4 b-c, the effect of lattice on the performance of various functions is different due to the dissimilar influence on resonances and BTW. The transmission modulated depth at f_L and f_H is increased/decreased depending on lattice match/mismatch, while the stability of the stable group delay switch is always boosted.

[1] Y. Hu, T. Jiang, J. Zhou, H. Hao, H. Sun, H. Ouyang, M. Tong, Y. Tang, H. Li, J. You, et al., *Advanced Optical Materials* **2019**, *7*, 22 1901050."